Oxid Met (2015) 84:211–231
DOI 10.1007/s11085-015-9551-6

ORIGINAL PAPER

Evaluation of the Mechanical Properties of Naturally Grown Multilayered Oxides Formed on HCM12A Using Small Scale Mechanical Testing

M. D. Abad[1] · S. Parker[1] · D. Frazer[1] · M. Rebelo de Figueiredo[1] · A. Lupinacci[1] · K. Kikuchi[2] · P. Hosemann[1]

Received: 20 February 2015 / Revised: 13 May 2015 / Published online: 7 June 2015

Abstract The microstructure and mechanical integrity of protective multilayered oxide films grown in liquid metal on F/M steel HCM12A was investigated utilizing Raman spectroscopy, nanoindentation and micro-cantilever testing methods. The Raman spectra showed a Fe_3O_4 outer layer and a Cr-rich spinel structure inner layer. The nanoindentation results showed a higher hardness value for the inner layer than for the outer layer. In addition, the hardness of the diffusion layer in between the inner layer and the bulk steel was measured. Quantitative fracture properties were obtained of the steel/oxide interface and within the oxide layers utilizing micro-cantilever testing. Furthermore the strength and elastic properties of the multilayered oxide film were measured and it was found that the porous structure in the inner Fe–Cr oxide limits the integrity of the steel/oxide interface.

Keywords Oxide coatings · Raman · Nanoindentation · Micro-cantilever · Fracture toughness

Introduction

Efficient heat transport fluids are of importance in many high power density applications, including advanced nuclear power. Liquid metal coolants, such as lead–bismuth eutectic (LBE) solutions, have many favorable qualities; however, it causes significant corrosion on common structural steels due to high dissolution rates [1–5]. To mitigate this corrosion phenomena, the dissolved oxygen content in the LBE may be limited by an intentional growth of a passivating oxide on the steel.

✉ S. Parker
scottparker@berkeley.edu

[1] Department of Nuclear Engineering, University of California, Berkeley, Berkeley, CA, USA

[2] Frontier Research Center for Applied Nuclear Science, Ibaraki University, Mito, Japan

If this oxide layer is stable under operation conditions, the lifetime of the steel substrate is limited either by the rate of oxide spallation from the surface of the substrate, or by the diffusion rate of alloying elements and oxygen throughout the oxide, as evaluated by [6–10]. Because this passive layer structure is the primary barrier against corrosive attack, comprehensive studies, like in [11–13], are designed to quantify and predict the integrity of multilayered oxides. Until recently, the mechanical failure of these oxide layers could not be measured because those oxides were too small to test: these measurements are now possible through advanced micromechanical materials testing techniques [14].

Characterizing the microstructure and material properties by such novel techniques is an important step forward in order to refine corrosion and erosion models. Erosion based materials degradation is important in high flow velocity applications, such as nuclear, oil, and gas field operations. Shear stresses on pipe walls are calculated using the simple approach $\tau_w = \mu\left(\frac{du}{dy}\right)$ where μ is the hydrodynamic viscosity, y is the distance from the pipe wall, and u is the flow velocity. However, it has been also found that this equation greatly under-predicts the stresses on a pipe wall and the freaky energy density (FED) model is more appropriate [15–18]. While the tools to evaluate forces on a pipe wall are developed, the tools to measure the actual strength of a passivation film have not been fully deployed yet. This work can be seen as an early approach utilizing advanced small scale mechanical testing for understanding the mechanical stability of thick passivation films and opens the door for the comprehensive use of this technique in corrosion science and engineering.

This investigation focuses on the properties of the oxide layers formed on ferritic martensitic (F/M) steel HCM12A in a liquid lead–bismuth eutectic solution for 5500 h at 450–500 °C. HCM12A has been selected because it is a promising candidate material for use in industrial heat transfer processes: it is one of the leading F/M steels for Generation IV lead-cooled fast reactors (LFR) reactors due to its high strength and favorable corrosion resistance [7, 19–22]. HCM12A is also a viable candidate for a range of other energy-producing applications, including solar thermal power facilities and gas turbine power systems [23, 24]. In both nuclear and non-nuclear applications, liquid metal coolants are under consideration as the primary heat transfer media [23–26]. High temperature oxidation of HCM12A in such extreme environments leads to the formation of a multilayered oxide structure, which have been studied previously on a range of different alloys [6–8, 27–30]. Oxide layers formed on HCM12A have been previously studied by scanning electron microscopy and energy dispersive X-ray spectroscopy (SEM/EDS), micro-X-ray diffraction (XRD), electron backscattered diffraction (EBSD), electron energy-loss spectroscopy (EELS), energy filtered transmission electron microscopy (EFTEM) and transmission electron microscopy (TEM) [19–22] and during exposure to LBE by SEM/EDX, EBSD, 3D atom probe tomography (APT) and scanning probe microscopy (SPM) [21, 31–33]. SEM/EDS combined with Raman spectroscopy have been used in this work to further study these oxide layers.

Schutze et al. [34] described a new approach towards the development of a comprehensive oxide scale failure diagram (OSFD) that delineates the mechanical

limits of scales for the different types of failure mechanisms. The authors concluded that although a number of experimental data already exists for establishing the new type of OSFD there is still need for further measurements and underlying understanding in order to make these diagrams more specific for the different material systems [34]. The mechanical properties of steel oxides and metal/oxide interfaces have been characterized before [34–38]. Few experimental techniques exist for micromechanical testing; such techniques allow the characterization of the discrete oxide layers, and only recently have these methods been applied to passivation films [14, 31, 39–45]. The oxide layers grown in a high temperature LBE environment are on the order of 10–30 μm thick; few conventional techniques for measuring mechanical properties have been developed for testing features on this scale. Nanoindentation in selected areas has been one of the main techniques in order to measure the hardness and reduced modulus [30, 31]. Micro-cantilever testing, developed by [14], was used to evaluate the elastic modulus and fracture strength of the oxide and steel/oxide interface grown on HCM12A in this work; few other technique offer the level of resolution and discrimination necessary to measure the mechanical properties of micro-scale features. The advantages of applying this technique to passivation films are that the sample geometry is well defined and the sample size is suitable for measuring discrete layers in the oxide [43]. Moreover, the mechanical properties of the multilayered oxides grown on HCM12A have been measured by localized nanoindentation and bend bar testing in-plane with the oxide layers and perpendicular to the layers in order to determine the discrete mechanical properties of each oxide layer and to evaluate the fracture mode and location.

Experimental Procedures

Material

HCM12A sample material was provided by Sumitomo Metal Industries, Ltd. The material is the same as described in [31–33]. The chemical composition of the steel is as follows (in wt%): 10.64 Cr; 0.3 Si; 0.61 Mn; 0.37 Mo; 0.14 C; 0.84 Cu; 1.94 W; 0.32 Ni; and 0.19 V. A cylindrical specimen was exposed to LBE solution for 5500 h at 450–500 °C at an oxygen content of 10^{-5} to 10^{-6} wt%. The details for the exposure are shown in [31–33].

Characterization Techniques

A FEI Quanta 3D FEG dual beam, which consists of a focused Gallium-69^{+} ion beam (FIB) and a SEM, has been used during this research. The chemical composition across the micro-cantilever was analyzed by EDS; line scans were conducted utilizing a 30 kV electron beam and an Oxford 20 mm Silicon Drift Detector (SSD). A scanning transmission electron microscopy (STEM) foil was prepared using ion milling in the Quanta 3D FEG. A Renishaw Invia Laser Raman spectrometer was used for the characterization. The excitation wavelength used was 488 nm line of an Ar^{+} ion laser at an incident power of 10 mW. The area was

analyzed using a 2 μm diameter spot through a standard 50× microscope objective. The spectra were collected with a 30/60 s data point acquisition time, a spectral range of 150–1000 cm^{-1} and a spectral resolution of 2 cm^{-1}.

Mechanical Properties

Several individual micro-cantilever bend bar specimens were manufactured on the oxide layers grown on the HCM12A sample in LBE. These bend bars were fabricated using a FEI Quanta 3D FEG focused Gallium-69^{+} ion beam (FIB), implementing the technique developed by Di Maio and Roberts [14]. Three different kinds of micro-cantilevers were manufactured: (1) In-plane with the oxide layer in the inner layer; (2) In-plane with the oxide layer in the outer layer; (3) Perpendicular to the oxide layers and extending from the bulk substrate to the edge of the outer layer. Since the micro-cantilever bars are fabricated in the oxide, the bend bar length on cross section specimens is limited by the thickness of the oxide layer. Additionally, the maximum load capacity of the indenter limits the total cross-section of the bend-bars.

The bend-bar tests were performed with a high-resolution PI-85 Hysitron indenter and a flat-punch diamond tip. The indenter and the sample were aligned with the Quanta 3D FEG: the setup was oriented such that the experiment could be observed in both the SEM and the FIB simultaneously. Displacement-controlled indentation tests were used to measure the force vs. displacement profile of the bend bars. The bend bars were loaded at a rate of 10–15 nm/s until fracture. SEM images were recorded before and after testing; the initial cross-sectional area and length of the bend bar were measured and used to calculate stress vs. strain profiles, from which the elastic modulus and fracture stress were determined. The bend bars had a rectangular cross-section. Samples prepared for fracture toughness measurements were notched, while bend bars tested for fracture stress and elastic modulus were not notched. Because the micro-cantilever bend bars deform elastically until fracture, the stress and strain may be calculated directly without finite element calculations. The strain at the fracture location was calculated using:

$$\varepsilon = \frac{6 \cdot z \cdot w(x) \cdot \Delta x_{\max}}{l^3} \tag{1}$$

where z is half the thickness of the bend-bar (μm), $w(x)$ is the displacement of the bend bar (μm), Δx_{max} is the maximum displacement of the bend bar at fracture (μm), and l is length of the bend bar (μm).

The stress was calculated using:

$$\sigma = \frac{F \cdot t \cdot z \cdot 10^{12}}{I} \tag{2}$$

where F is the applied force (N), t is the distance between the line of action of the applied force and the base of the bend bar (μm), z is half the thickness of the bend bar (μm), and I is the moment of inertia for a rectangular cross section (μm^4). The elastic modulus was determined experimentally from the slope of the stress strain

curve. In order to measure the fracture toughness (K_{IC}), a sharp precursor crack was milled with the FIB prior to testing select bend bars, according to the technique described in Di Maio and Roberts [14]. The fracture toughness was then calculated using the following equation:

$$K_{IC} = \sigma_{fracture} \cdot F(a/b) \cdot \sqrt{\pi \cdot a_c} \tag{3}$$

where $\sigma_{fracture}$ is the stress at fracture (MPa), a is the depth of the FIB-milled notch (m), and the shape factor, $F(a/b)$ is defined as follows:

$$F(a/b) = 1.22 - 1.22(a/b) + 3.74(a/b)^2 + 3.873(a/b)^3 - 19.05(a/b)^4 + 22.55(a/b)^5 \tag{4}$$

where a is the depth of the pre-notched crack, and b is the thickness of the bend bar. The bend bars were on the order of 15–20 μm long, with a 5 × 5 μm cross section.

Nanoindenation was performed on the sample. The nanoindenter tip was calibrated using fused silica prior to the measurements. The calibration leads to an area function correcting for geometrical inconsistencies in the used diamond tip. The indents were performed at 1 mN/s loading rate, 2 mN/s unloading rate and 30 s dwell time. They were placed 5 μm apart and offset maximum depth was 300 nm. The nanoindentation experiment was carried out using the depth vs. load hysteresis with indents being terminated using depth control. The thermal drift correction data was collected post-indentation. The nanoindentation hardness (H_{berk}) and reduced indentation modulus (Er) were calculated from the indents utilizing the Oliver and Pharr method [46]. A total of 86 indents have been performed on the sample.

Results

SEM/EDX and Raman Spectroscopy

As described in [31–33], two distinct oxide layers were found to have evolved on the surface of the HCM12A sample. These works suggested the formation of an outer Fe_3O_4 layer and a Cr-rich iron oxide spinel (or $Fe_{3-x}Cr_xO_4$), and a diffusion zone separating the Fe–Cr spinel from the substrate steel. A representative SEM image and EDS line scan are shown in Fig. 1. In the SEM image (Fig. 1a), the sample surface exposed to LBE is on the left; the un-oxidized steel is on the right. Notice that the first two micrometers consist of Pb/Bi. The Pb/Bi is remnant contamination from the LBE solution in which the oxide layers were grown. The layered structure is clearly visible and consists of the following zones, measured in from the surface: outer oxide (2–12 μm), inner oxide (12–18 μm), inner diffusion zone (18–23 μm), and steel. The EDS scan line in Fig. 1b shows that the outer layer consists of Fe and O. A significant amount of Cr was detected in the inner layer, with a corresponding decrease of the Fe content compared to the outer layer. In the diffusion layer, the O content decreases abruptly and is not observed in the steel substrate. Moreover, an increase of Fe and decrease of Cr, representative of the nominal composition, are observed further in sample. Large pores are clearly

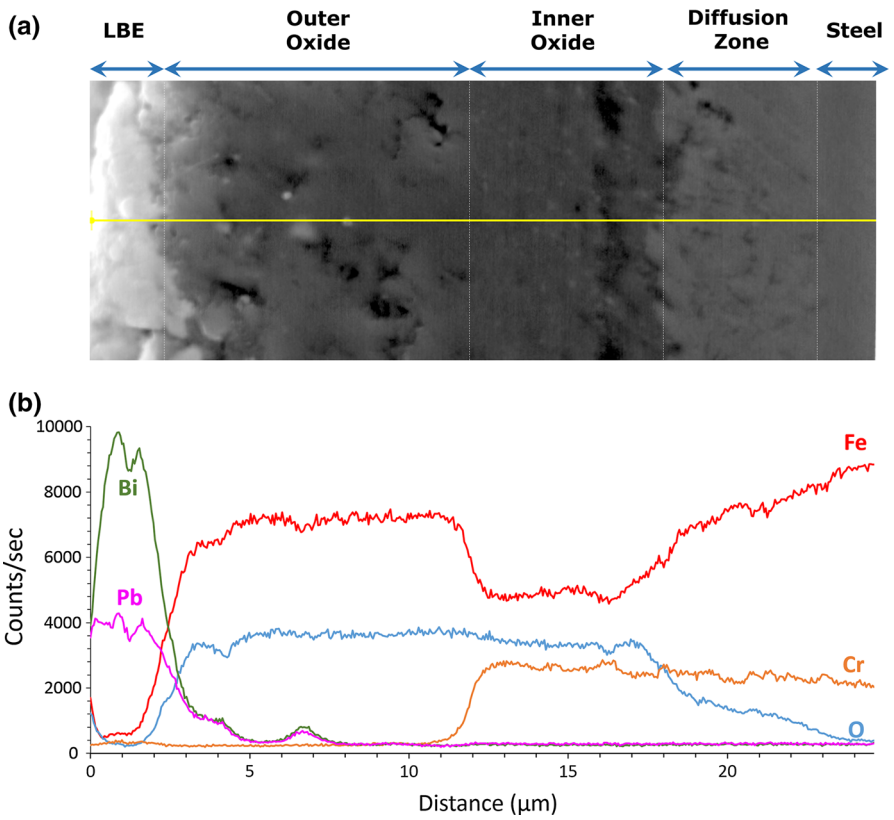

Fig. 1 **a** SEM image of the cross-section of oxide layers formed on HCM12A after exposure to LBE for 5500 h at 450–500 °C. **b** EDS Line Scan. The sample surface exposed to LBE is on the *left*; the un-oxidized steel is on the *right*

observable on the outer layer, and in region closest to the diffusion layer in the inner oxide.

While 3D APT and SPM were used to characterize the oxide layers [32, 33], neither XRD nor other phase characterization techniques have been performed in order to confirm the exact composition of these regions in the oxidized layers after LBE exposure of the HCM12A. Our results suggest the formation of an outer Fe_3O_4 layer and a Cr-rich iron oxide spinel (or $Fe_{3-x}Cr_xO_4$ with $0 \leq x \leq 2$ [47]). Raman spectroscopy was used to confirm the composition of each region, as it has been used by several authors in similar studies [48–51]. The outer and inner oxide layers were analyzed by Raman spectroscopy (10 mW—30 s) and the spectra are plotted in Fig. 2a. The absence of sharp, well defined peaks could be attributed to the local structural disorder of the oxides [52]. The spectra from the outer layer shows several broad bands. The band with the biggest intensity is found at 666 cm^{-1} and it is associated with the A_{1g} vibration mode of the Fd-3 m structure of magnetite. Bands at 535, 302 and 194 cm^{-1} are observed and associated with the $T_{2g(3)}$, E_g and $T_{2g(1)}$

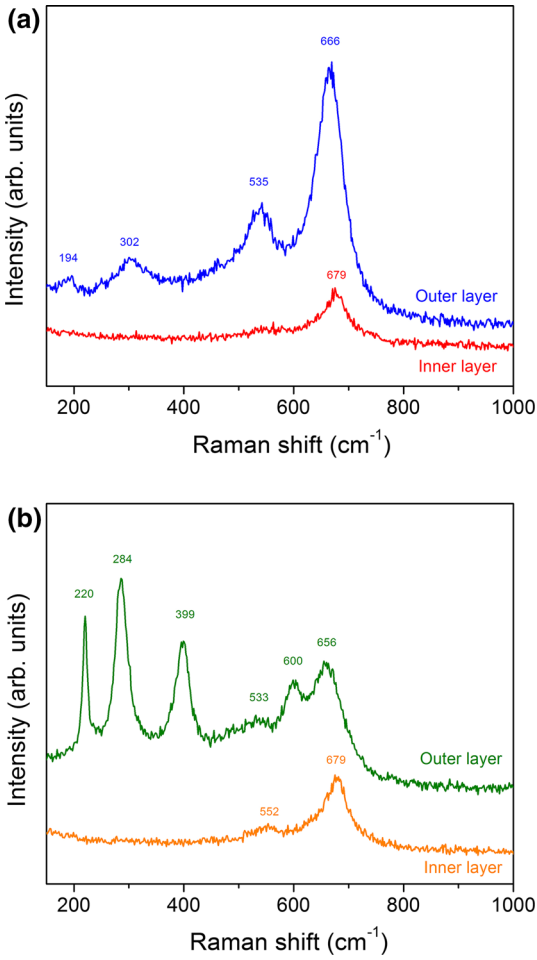

Fig. 2 Raman spectra from the outer and inner oxide layers at: **a** 10 mW—30 s and **b**—60 s aquicistion time

vibration mode respectively from the magnetite [53–55]. The usual A_{1g} vibration mode has been located between 667 and 671 cm^{-1}. The main values for the different main vibration modes of Fe_3O_4 from the literature have been plotted in Table 1 in order to compare with the obtained results. There is a clear correlation in the results reported from other authors and this work.

The Raman spectra of the inner oxide layer is shown in Fig. 2a and it is clearly different from the outer layer. Both spectra have been taken under the same conditions, however, a lower intensity is found and a clear broad band could be observed around 679 cm^{-1}. On the basis of the Fe_3O_4 results, the band around 679 cm^{-1} is associated with the A_{1g} vibration mode of the $Fe_{3-x}Cr_xO_4$ ($0 \leq x \leq 2$). The three weaker phonons ($T_{2g(3)}$, E_g and $T_{2g(1)}$) in Fe_3O_4 are not observed in the present spectra: there is barely a broad band (if any) associated with the $T_{2g(3)}$ mode. It has been noticed that this biggest Raman band is slightly shifted to higher frequencies than the theoretical values for the same A_{1g} vibrations mode,

Table 1 Vibration modes and Raman shift found in this work in the different oxide layers and in similar works

	Symmetry and Raman shift (cm^{-1})				Description of the samples	Reference
	$T_{2g(1)}$	E_g	$T_{2g(3)}$	A_{1g}		
Outer layer Fe_3O_4	194	302	535	666	Corrosion of HDM12	This work
	193	306	538	668	Natural magnetite	[54]
				671	Grinding and heating treatment	[47]
		300	543	670	Product of corrosion (no material specified)	[52]
		300	550	670	Annealing of thin films	[53]
	193	308	540	670	Redox reactions	[55]
		295	531	667	Combustion and redox reactions	[50]
		306	530	668	Corrosion of HT9	[50]
		306	537	669	Corrosion of D9	[50]
		306	532	667	Corrosion of 316L	[50]
Inner layer [$Fe_{3-x}Cr_xO_4$ ($0 \leq x \leq 2$), or Cr-rich Fe oxide]				679	Corrosion of HDM12	This wok
				686	Grinding and heating treatment	[47]
			531	678	Combustion	[50]
			509	679	Corrosion of HT9	[50]
				672	Corrosion of D9	[50]
			514	673	Corrosion of 316L	[50]

670–672 cm^{-1} [47, 53, 56, 57] of the Fe_3O_4. Similar findings have been reported by Hosterman [50] and McCarty et al. [47]: that is to say, there is a shift to higher frequencies, a faint band around 535 cm^{-1}, and the dissapearance of any other features (Table 1). It has been reported by McCarty et al. [47] that the formation of $FeCr_2O_4$ or any other non-stoichiometric $Fe_{3-x}Cr_xO_4$ compound [47, 50, 56, 57] could shift the A_{1g} band to higher frequencies. Hosemann et al. probed the formation of a Cr-rich iron oxide in D9 steel under LBE corrosion process by TEM [6] and the same shift was reported [50].

Optimization of laser power and acquistion time is vital for collecting magnetite Raman spectra as phase changes are easily induced by the excitation laser [53]. At acquisition times longer than 30 s and 10 mW laser power, hematite features were observed in collected spectra. Figure 2b shows the spectra collected with the same power, but with 60 s of acquisition time. The spectra taken on the outer layer shows the typical peaks from Fe_2O_3 and Fe_3O_4. The peaks found at 222, 284, 399 and 600 cm^{-1} are the peaks associated with the $A_{1g(1)}$, $E_{g(3,4)}$, $E_{g(5)}$, $E_{g(5)}$ vibration modes, respectively, from the hematite Fe_2O_3 [58, 59]. The peaks at 533 and 656 cm^{-1} are attributed to Fe_3O_4. Similar phase transformation from Fe_3O_4 to Fe_2O_3, has been reported by Hostermann and Jubb et al. with an intermediate phase

(maghemite) speculated to be induced by the laser [50, 53]. However, Shebanova et al. did not observed the maghemite phase or a laser induced transformation [54]. The spectra collected under the same conditions in the inner layer did not show any change with the increasing laser power. No phase change was observed in the inner layer: there is a higher intensity signal and a small shoulder at 635 cm^{-1} associated with the $F_{2g(4)}$ vibration mode of $FeCr_2O_4$ [60]. It is believed that the substitution of Fe, from the inverse spinel Fe_3O_4, for Cr to form the spinel structure decreases the phase induction to Fe_2O_3.

Nanoindentation

The mechanical properties, hardness (H_{berk}) and reduced modulus (Er), were evaluated in cross-section in order to measure the hardness of the different layers. 2D dimensional hardness maps of the material were gained and plotted in 3D with the H_{Berk} and Er on the Z-axis, as can be seen in Fig. 3a, b respectively. The left part is the closest part to the LBE, and then the right part is the steel. In these 3D maps,

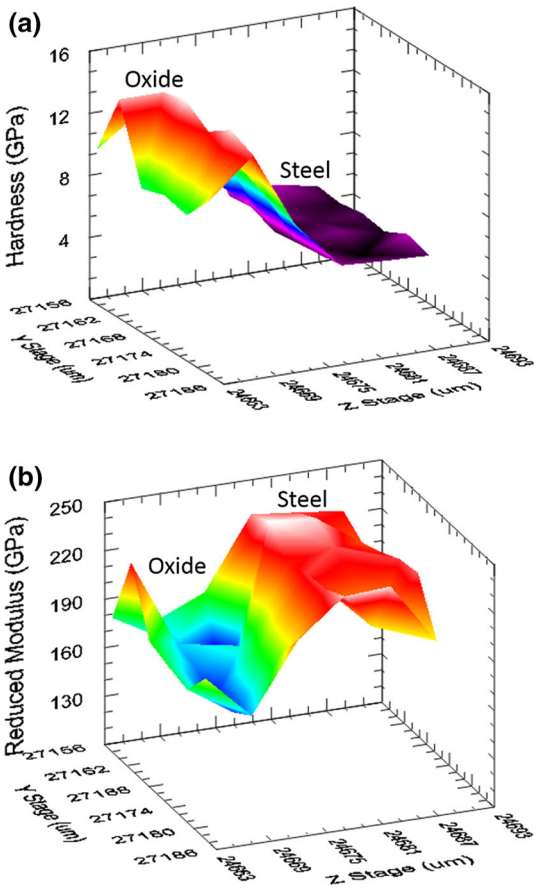

Fig. 3 3D maps of the different regions obtained: **a** hardness, and **b** reduced modulus. The *left* part is the closest part to the LBE, and then the *right* part is the steel

the differences in H_{Berk} and Er as a function of the measured region are clearly seen. The post indentation analysis by SEM is shown in Fig. 4a. Since the location of each individual indent was located utilizing SEM, all hardness data can be summarized in Fig. 4b and the words *outer*, *inner*, *diffusion* and *steel* have been used to indicate the location of the indents. Three different fields of indents 3D maps have been carried out on the sample, and post indention SEM guarantees accurate position of the indents on the sample. A small influence from the neighboring nanoindentation could not be discarded in the steel region.

Some authors have considered the "diffusion layer" as a unique layer, such as [19, 20], due to the different structure of the inner layer and the bulk; others have not differentiated this layer as being different from the bulk [21, 31]. In this work, for the chemical bonding and microstructural analysis, only two layers have been considered (outer and inner). However, for the nanoindentation portion of this work, a third layer has been distinguished. Previous research in this material by Yamaki and Kikuchi [31] did not distinguish this layer. In this research, the diffusion layer has been considered as a layer of interest. The values of the H_{Berk} and Er as a function of the location have been plotted in Fig. 4b. On average, the outer layer (10 GPa) is significantly softer than the inner layer (13 GPa). The diffusion layer shows

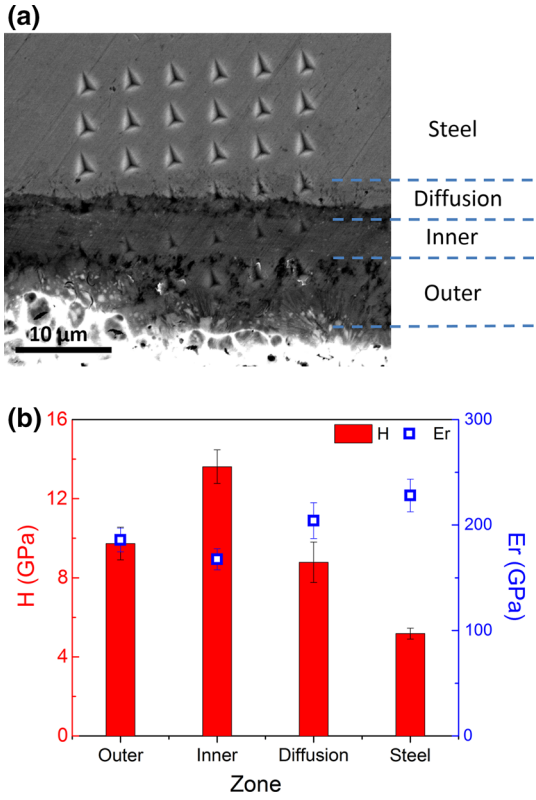

Fig. 4 **a** SEM with the location of the imprints and different regions detailed and **b** H_{Berk} and Er found out in each region

a decrease of the H compared with the inner layer, and an increase of the Er. The diffusion layer trends to be similar to the steel substrate further in the sample.

Mechanical Properties by Micro-Cantilevers

Several micro cantilevers were manufactured on the oxide layers: there are samples in the inner layer, outer layer, and perpendicular to the oxide layer extending from the bulk substrate to the edge of the outer layer (as described in "Mechanical Properties" section). A SEM image of the grown oxide with a schematic representation of the orientation of the bend bars is shown in Fig. 5. Samples prepared for fracture toughness measurements were notched (in the inner and outer layers), while bend bars tested for fracture stress and elastic modulus evaluation were not notched (in the inner and outer layers and the cross-section micro-cantilevers). A list of all the cantilevers tested in this work is found in Table 2. The designation "I#" indicates a cantilever test in the inner oxide, "O#" corresponds with tests in the outer oxide, and "C#" corresponds with cantilevers manufactured in cross-section.

Figure 6a shows a SEM image taken during the in situ micro-cantilever I2 test on the inner oxide layer. The sample and indenter orientation are shown in Fig. 6a. Figure 6b presents the resulting fracture surface of the inner layer after I1 test. Figure 6c shows one of the micro-cantilevers tested in the outer layer (O1) at the moment of the fracture. This micro-cantilever did not break at the notch, rather, the fracture path is several μm away. This happened for one of the two tested micro-cantilevers. Figure 6d shows the resulting fracture in O2 outer layer micro-cantilever. No plastic deformation was observed in either the inner layer or the outer layer and it can be seen from the sharp crystalline fracture surface that both inner and outer oxide fractured in a brittle mode. The fracture mechanism, however, clearly varies as a function test location: the post-fracture SEM image on the inner and outer oxide layer shows that the outer oxide layer fractured in the intercrystalline mode, as evidenced by the clear crystalline boundaries, while the inner oxide layer fractured in the transcrystalline mode. In addition, small Kirkendall pores (<10 nm) were observed on the fracture surfaces of the inner oxide layers, which were also observed in [61]. Figure 6e shows a typical micro-cantilever prepared on the cross section (C1) (not notched) and in Fig. 6f shows the

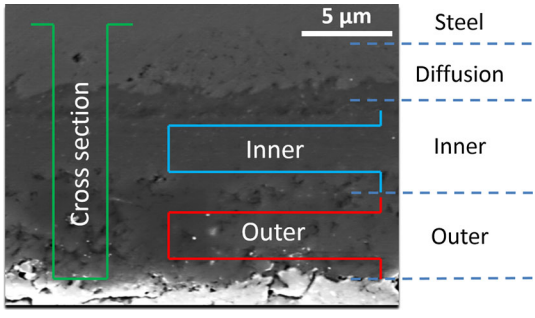

Fig. 5 SEM image of the grown oxide with a schematic representation of the orientation of the bend bars

Table 2 Mechanical properties obtained in the different regions

	Nanoindentation			Number of indents	Cantilever	Micro-cantilevers							
	H_{Berk} (GPa)	Er (GPa)	E (GPa)			Label	Notched	Fracture stress (MPa)	Failure strain (%)	$K_{Ic}(MPa\sqrt{m})$	E (GPa)	Average K_{IC} $(MPa\sqrt{m})$	Average E (GPa)
Outer layer	9.7 ± 0.8	185.8 ± 11.3	200.5 ± 10.3	13	Outer layer	O1	Yes	1300	2.7	1.23	48.3	1.14 ± 0.13	50.4 ± 2.9
						O2	Yes	1100	5.4	1.05	–		
						O3	No	1620	3.7	–	52.4		
Inner layer	13.6 ± 0.8	167.5 ± 10.0	177.3 ± 9.2	19	Inner layer	I1	Yes	1620	4.2	1.54	–	1.49 ± 0.07	143.2 ± 19.9
						I2	Yes	1520	3.6	1.44	–		
						I3	No	1440	0.9	–	150.1		
						I4	No	1510	1.3	–	120.7		
						I5	No	1630	1.0	–	158.7		
Diffusion layer	8.8 ± 1.0	204.2 ± 17.0	224.6 ± 15.6	13	Cross section	C1	No	1470	1.1	–	137.4		194.0 ± 61.8
						C2	No	1390	0.8	–	184.7		
						C3	No	1320	0.5	–	259.9		
Steel	5.2 ± 0.3	228.0 ± 15.4	257.3± 14.1	46									

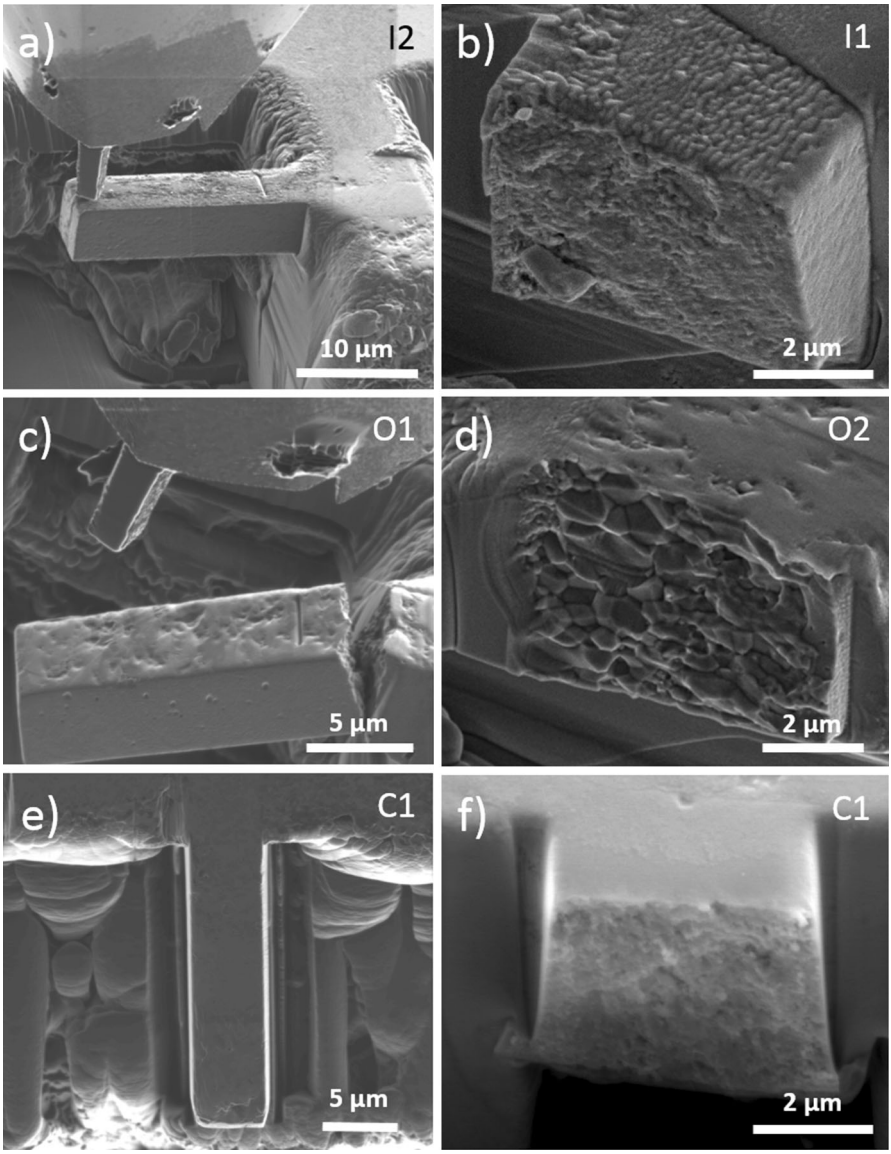

Fig. 6 **a** Microcantilever setup, as viewed from the FIB: the indeter is positioned vertically above the bend bar (I2) fabricated in the inner oxide. **b** Post testing fracture surface of an inner oxide layer bend bar (I1). **c** Fracture moment of the microcantilever on the outer layer (O1). **d** Post testing fracture surface of an outer oxide layer bend bar (O2). **e** Top view of a microncatilever fabricated perpendicular to the oxide layers (C1). **f** Fracture surface of microcantilever C1. The designation "I#" indicates a cantilever test in the inner oxide, "O#" corresponds with tests in the outer oxide, and "C#" corresponds with cantilevers manufactured in cross-section

fracture surface after the test. This micro-cantilever was made perpendicular to the grown oxide layer and extends from the bulk steel, across the inner layer, and ends in the outer oxide layer, as shown in Fig. 5. The micro-cantilever fractured in the inner part of the inner layer where a porous region was detected. The found porosity in the closer region to the diffusion layer will be explained further in the text.

Applying Eq. (1) and (2), the stress vs. strain curves have been calculated for each test, and the values of the fracture stress and failure strain have been plotted in Table 2. In Fig. 7a the values of the fracture stress for each test have been plotted (the notched micro-cantilevers are plotted with stripped bars and the no-notched micro-cantilevers in solid bars). No big differences have been found in the fracture stress among the different bars, just a slight decrease in the case of the notched cantilevers in the outer layer. The stress–strain curves obtained from the notched cantilevers have been plotted in Fig. 7b. The curves obtained from the inner layer are very similar, however, the outer layer showed significant scattering of the measured data. The fracture toughness for each notched micro-cantilever has been determined and plotted in Table 2. As can been seen, the average value of the K_{Ic} from the inner layer is slightly higher (1.49 ± 0.07 MPa*$\sqrt{m}$) than the outer layer (1.14 ± 0.13 MPa*$\sqrt{m}$). In Fig. 7c, the stress vs. strain curves obtained from the not-notched micro-cantilevers have been plotted. The curves obtained from the micro-cantilevers made on the inner layer are very similar to the curves obtained from the cross-section micro-cantilevers. However, a big difference is observed in the case of the outer layer, as seen in the notched micro-cantilevers used for calculating the fracture toughness. The Young modulus for each micro-cantilever and the average for each family has been plotted in Table 2. The inner oxide had an average elastic modulus of 143 GPa, while the elastic modulus from the cross section bars was 194 GPa. The outer oxide layer showed a value of 50 GPa. No plastic deformation was observed in either oxide layer or the micro-cantilever tests performed in cross section; this is shown by the linear slope of the stress vs. strain plots in Fig. 7b and c. The inner oxide layer, which has been shown to grow inward, has a greater mechanical integrity than the outer oxide layer, which grows outward of the original surface. This observation confirms findings as described in Yamaki and Kikuchi [31].

Discussion

Analysis of HCM12A steel corroded in a high temperature, oxygen-controlled, LBE environment, was performed by comparing the EDX and Raman spectra from the different corrosion layers of the steel samples. EDX and Raman spectroscopy suggested the formation of an outer Fe_3O_4 layer and a Cr-rich iron oxide spinel (or $Fe_{3-x}Cr_xO_4$ ($0 \leq x \leq 2$)) in the inner layer. Similar phases have been found by Hosemann et al. [6] in oxide layers grown on D9 by TEM. Moreover, the inner layer showed a high porosity. Bischoff and Motta [19, 20] found similar phases in layers grown in HCM12A under SCW process by EELS/EFTEM and TEM. Tan et al. studied the differences in the oxide layers in HCM12A grown under SCW and LBE and small differences were found [21]. In general, the outer layer consist of a

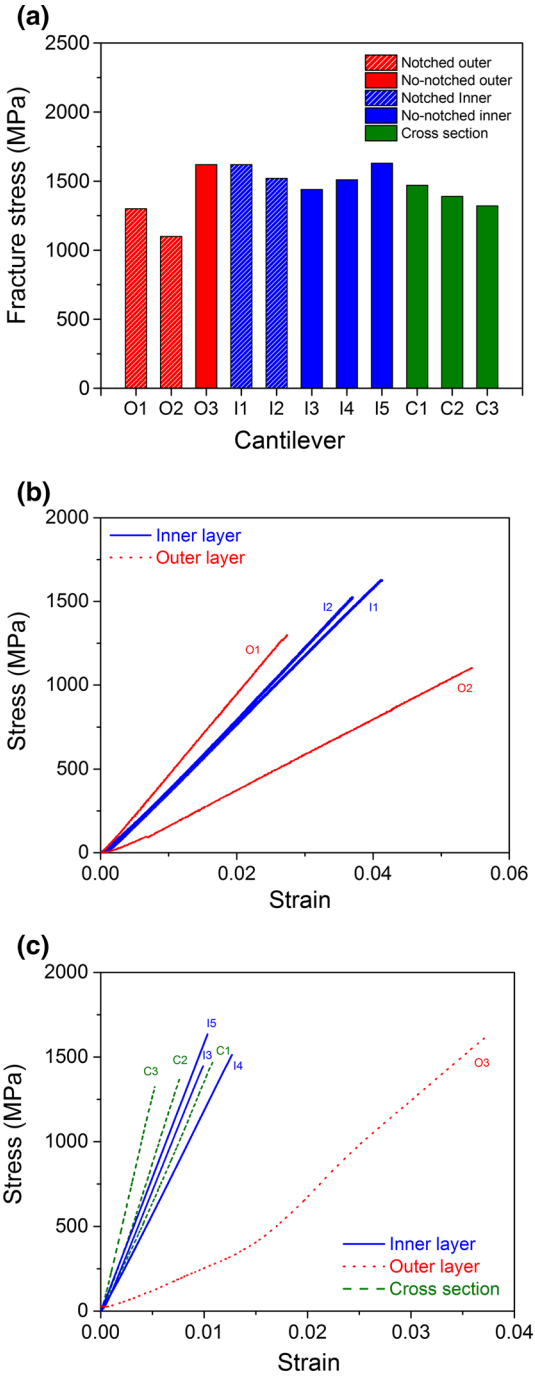

Fig. 7 **a** Fracture stress values calculated for each cantilever. **b** Stress versus displacement curves for the notched cantilevers. **c** Stress versus strain curves for the not-notched cantilevers

magnetite Fe_3O_4 phase and it is very coarse due to the discontinuous columnar-like structure that grew with LBE inclusions and microvoids [31, 33]. The inner layer is mainly Cr-rich spinel, or $Fe_{3-x}Cr_xO_4$, with a very flat surface; small micro-voids are observed near the inner oxide– substrate interface. It is known that the outer layer grows outward from the original surface while the inner layer grows inward as shown in [6] which results in movement of Fe towards the outer layer. It has been suggested that the porosity found in the inner layer is due to different diffusion constants of the inward-diffusing oxygen and outgoing Fe, and the resulting porosity is the result of the Kirkendall effect.

The results obtained by nanoindentation are very similar with the results published by Yamaki and Kikuchi [31]; outer layer ($H_{Berk} \sim 10$ GPa. $E \sim 234$ GPa), inner layer ($H_{Berk} \sim 10$ GPa and $E \sim 210$ GPa) and the bulk substrate ($H_{Berk} \sim 5.5$ GPa and $E \sim 260$ GPa). It is noticeable the bigger hardness value obtained in the present work for the inner layer (13.6 GPa). However, the values provided by Yamaki and Kikuchi are in agreement with the average value of the inner and diffusion layer combined. It is believed that, due to the fact that the author did not distinguish the two layers, only the average value was reported. Hosemann et al. [30] had observed similar behavior in oxidation layers from D9 steel after 2000–3000 h in LBE, where the biggest values of hardness are found in the inner layer together with a small decrease in E-modulus.

The fracture toughness measured by micro-cantilevers show very similar results for both the outer and inner layer. However, the outer layer showed a lower value of K_{IC} and a higher standard deviation. A value of 1.1 MPa*$\sqrt{}$m was found for iron oxides grown in air at 550 °C by Nagl et al. [37], which is comparable to our findings of 1.14 and 1.49 MPa*$\sqrt{}$m for the outer and inner layer, respectively. A large range in fracture toughness values was found by micro-cantilevers in Ni-W alloys by Armstrong et al. [62] and it was also attributed to the sample porosity. It is believed that the porosity of the outer layer could affect the measurements.

The elastic modulus values are lower than the values found by nanoindentation for Fe_3O_4 and Fe–Cr spinel oxide layers. This difference is pronounced in the outer layer. It seems likely that measured differences in the mechanical properties are due to the fact that the material is not fully dense. While the outer oxide layer did not contain a significant amount of small pores, it contained large pores and significant LBE inclusions. The larger bend bar geometry is more likely to sample some amount of these inclusions than the smaller nanoindentation volume. Nagl et al. pointed out that the void size was critical for comparing failure strain with predictions based on a fracture mechanics model [37]. Jauffres et al. investigated fracture mechanics of porous ceramics and concluded that increasing the porosity drastically reduces their strength leading to failure issues [63]. The mechanical properties, such as H_{Berk} and K_{Ic}, of the outer layer are lower than the inner oxide. In addition, the outer oxide layer fractures in an intercrystalline mode, which indicates that the grain boundaries contribute to lower strength. Mueller et al. observed similar slight differences between two values of K_{Ic} measured in alumina fibers and suggested that it could be because of the differences between transgranular and intergranular fracture [64]. Since the oxide layer is growing while exposed to flowing LBE, it is likely that small amounts of LBE migrate into

the grain boundaries. Tan et al. [21] found that the porous outer layer was more easily removed. The inner layer also showed a lower value than the value obtained by nanoindentation, but the difference is not as significant. The inner layer had numerous small pores, which could affect the obtained values by micro-cantilevers. The values obtained from different modes (from loading curve in the micro-cantilevers and unloading curve in nanoindentation) could have a significant difference in porous samples. Recent findings by Frazer et al. [65], however, showed a good agreement between the mechanical properites measured by nanoindentation of micro-cantilevers in fully dense SiC, which confirms that change due to FIB damage is neglidibly small in these geometries.

Considering the results obtained by the cross section micro-cantilevers, the cross section micro-cantilevers did not break at the inner oxide layer/steel interface where the applied torque is highest, but rather 1–2 μm in the inner oxide layer. The value of E-modulus found in this cross-section micro-cantilevers was higher than in the outer or inner layer, however, the standard deviation was higher too. A SEM image of the remaining portion of a micro-cantilever with an EDS Line Scan superimposed are shown in Fig. 8a and b respectively. It can be seen that the micro-cantilever fractured in the inner oxide just before the diffusion zone, rather than at the base of the micro-cantilever where the bending moment is highest. The E-modulus was found to be 194 GPa for this kind of micro-cantilever, which agrees with the value of the E-modulus found for the region in between the inner and diffusion layer (177 GPa and 224 GPa respectively). 3D atom probe analyses were employed by Kikuchi et al. [33] for stoichiometry measurement of Fe, Cr, O and Si at the Fe–Cr spinel layer near the boundary of magnetite and spinel. They detected super enrichments of Cr with a size of approximately 10 nm, as well as depletion of Fe and an enrichment of O at the same site. However, these findings did not affect the micro-cantilever testing because the fracture of the micro-cantilever was found in the inner layer at 1 μm far away from the diffusion zone. The moment at the fracture site was 40 % less than the maximum moment at the base of the bend bar. Close to the fracture site many pores were found in the SEM image in Fig. 8a. Upon close examination in Fig. 1 and in Fig. 4a, it can be seen that the location of fracture in cross section is at an area of high pore density in the inner oxide layer. It is notable that Yamaki and Kikuchi found, after ring compression, cracks across the oxide layers from the interface between the oxide layer and the base metal to the surface of oxide layers, and the delamination of oxide layers occurred at the Fr–Cr spinel layer [31].

A STEM foil evaluated in transmission mode using the SEM/FIB was prepared and investigated. A SEM image of an ion-milled cross-section of the passivation layer is shown in Fig. 9. The different regions are observed clearly on the prepared foil. Small pores are found in the inner oxide layer, but a high density porous structure is observed approximately 2 μm away from the steel substrate. The fracture site, shown in Fig. 8 and in Fig. 6f, occurs within the region of this porous structure. This region of high density of pores has also been observed by Bischoff et al. [19]. The author showed the same oxidation process occures after exposure to SCW on different steels. The author found a similar two layer structure (mainly outer layer, inner layer, and a diffusion layer). The inner layer contains primarily an iron-chromium spinel phase with a composition that ranges from Fe_3O_4 to $FeCr_2O$

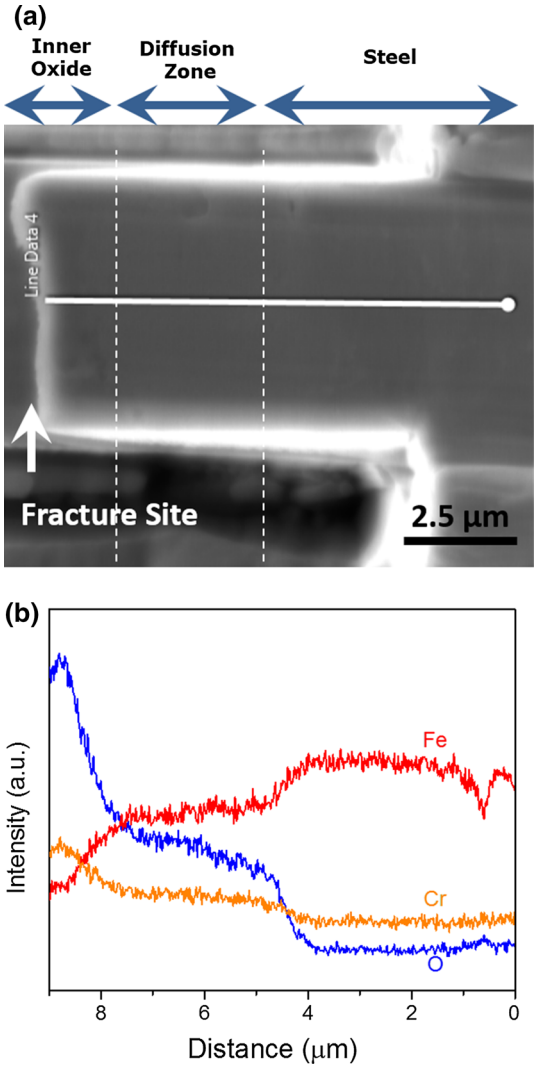

Fig. 8 **a** Post-testing SEM and **b** EDS Line Scan superimposed of the remaining portion of a bendbar fabricated in cross-section for the layered oxide structure

(in the closest region to the diffusion layer). The formation of the larger pores is explained as a function of the oxide advancement along the boundaries from the bulk, as is observed in SCW and steam corrosion processes [19]. We believe that similar processes are at work in LBE, but with different oxygen concentrations. In [20] it is reported that the porosity of this inner Cr-rich layer suggests that the pores originate from the outward migration of iron. Both the inner oxide and the diffusion layer exhibit a complex structure with a non-unifurm distribution of elements, as seen by SEM/EDX in this work and by Kikuchi et al. [31–33], as well as by APT and STM. It appears that the diffusion layer plays an active role in slowling down the outward diffusion of Fe and therefore influences the corrosion behaviour [20]

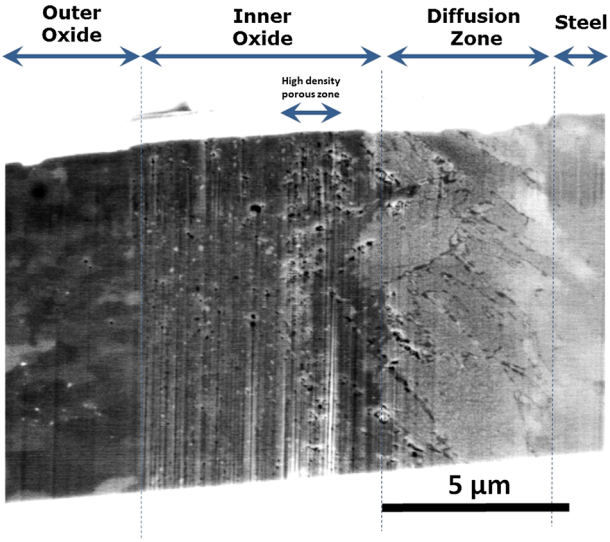

Fig. 9 SEM image of an ion-milled cross-section of the passivation layer

and the mechanical properties as seen by microcantilevers and ring compresion [31].

In summary, two oxide layers have been identified; an outer layer of Fe_3O_4 with a highly porous structure and a complex inner layer with many, small pores and $Fe_{3-x}Cr_xO_4$ spinel structure. The mechanical properties found out by micro-cantilever were influenced by the porosity of both layers. In the inner layer, closer to the diffusion zone, a high density of medium size pores was found. This high pore density was resposible for the fracture of the cross-section bend bars.

Quantification of the mechanical properties of the layered oxide structure on HCM12A provides valuable insight into how oxides might be removed from the substrate and provides useful feedback for finite element modeling of oxide spallation into liquid metals. While the solubility is inherent to the chosen liquid-structure couple, a potential approach for managing the integrity of the oxide is to control the partial pressure of oxygen in the liquid phase so as to control the growth and removal of the passive layer for the corrosion phenomena associated with LBE solutions at high temperature. It would seem that reducing the porosity in the inner oxide would certainly enhance corrosion resistance.

Conclusions

In summary, Raman spectroscopy has been carried out in the different oxide layers to confirm the Fe_3O_4 magnetite phase in the outer layer and the $Fe_{3-x}Cr_xO_4$ ($0 \leq x \leq 2$) spinel structure in the inner layer. The hardness, elastic modulus, fracture stress, fracture type, and fracture nucleation were determined for the layered oxide structure grown on HCM12A by the successful application of micro-

mechanical testing. It was demonstrated that micro-cantilever testing on discrete oxide layers grown at high temperature in LBE solution can be conducted with a high degree of reproducibility. The outer oxide layer appears to fracture in an intercrystalline mode while the inner oxide layer fractures in a transcrystalline mode. The lower values obtained by micro-cantilevers are attributed to the porosity of the grown oxide layers. The findings suggest that the crack initiation site, and the strength-limiting feature, is a region of nano-pores distributed in the inner oxide, approximately 2 μm from the oxide/substrate interface.

Acknowledgments The Authors thank the NRC faculty development grant NRC-38-09-948 for providing funding for this work. This material is based upon work supported by the Department of Energy under Award Number DE-EE0005941 as well as the nuclear energy university program (NEUP). The authors would also like to thank Biomolecular Nanotechnology Center (BNC) at UC Berkeley for the use for the SEM/FIB facilities.

References

1. J. Zhang and N. Li, *Corrosion Science* **49**, 2007 (4154).
2. J. Zhang and N. Li, *Journal of Nuclear Materials* **373**, 2008 (351).
3. D. Frazer, E. Stergar, C. Cionea and P. Hosemann, *Energy Procedia* **49**, 2014 (627).
4. V. Tsisar, C. Schroer, O. Wedemeyer, A. Skrypnik and J. Konys, *Journal of Nuclear Materials* **454**, 2014 (332).
5. L. Martinell, F. Ballbaud-Celerier and A. Teriain, *Corrosion Science* **50**, 2008 (2549).
6. P. Hosemann, R. Dickerson, P. Dickerson, N. Li and S. A. Maloy, *Corrosion Science* **66**, 2013 (196).
7. P. Hosemann, C. Hofer, G. Hlawacek, N. Li, S. A. Maloy and C. Teichert, *Journal of Nuclear Materials* **421**, 2012 (140).
8. J. Zhang, P. Hosemann and S. A. Maloy, *Journal of Nuclear Materials* **404**, 2010 (82).
9. J. Zhang, N. Li and Y. Chen, *Journal of Nuclear Materials* **342**, 2005 (1).
10. F. J. Martin, L. Soler, F. Hernandez and D. Gomez-Briceno, *Journal of Nuclear Materials* **335**, 2004 (194).
11. V. Shankar, J. Rao and I. Lim, Soon Hwang, L.K. Singhal. *Corrosion Science* **63**, 2012 (113).
12. E. Yamaki, K. Ginestar and L. Martinelli, *Corrosion Science* **53**, 2011 (3075).
13. C. Schroer, A. Skrypnik, O. Wedemeyer and J. Konys, *Corrosion Science* **61**, 2012 (63).
14. D. Di Maio and S. G. Roberts, *Journal of Materials Research* **20**, 2005 (299).
15. C. Kapsalis, G. Schmitt, R.Feser, B. Sagebiel, S. Wilmes, M. Macziek, New Investigations on Critical Wall Shear Stresses of CuNi Alloys in Natural and Artificial Seawater. EUROCORR (Stockholm 11).
16. G. Schmitt and M. Bakalli, in *Shreir's Corrosion*, vol. 2, 4th ed, eds. J. Richardson, et al. (Elsevier, Amsterdam, 2010), pp. 954–987.
17. G. Schmitt and M. Bakalli, *Power Plant Chemistry* **9**, 2007 (89).
18. G. Schmitt and M. Bakalli, *Materials and Corrosion* **59**, 2008 (181).
19. J. Bischoff and A. T. Motta, *Journal of Nuclear Materials* **424**, 2012 (261).
20. J. Bischoff and A. T. Motta, *Journal of Nuclear Materials* **430**, 2012 (171).
21. L. Tan, M. T. Machut, K. Sridharan and T. R. Allen, *Journal of Nuclear Materials* **371**, 2007 (161).
22. P. Ampornrat and G. S. Was, *Journal of Nuclear Materials* **371**, 2007 (1).
23. C. Forsberg, *Progress in Nuclear Energy* **47**, 2005 (32).
24. T. Mizuno and H. Niwa, *Nuclear Technology* **146**, 2004 (155).
25. L. Brissonneau, F. Beauchamp, O. Morier, C. Schroer, J. Konys, A. Kobzova, F. Di Gabriele and J.-L. Courouau, *Journal of Nuclear Materials* **415**, 2011 (348).
26. J. S. Zhang and N. Li, *Nuclear Technology* **144**, 2003 (379).
27. L. Martinelli, F. Balbaud-Célérier, A. Terlain, S. Bosonnet, G. Picard and G. Santarini, *Corrosion Science* **50**, 2008 (2537).
28. L. Martinelli, F. Balbaud-Célérier, G. Santarini, G. Moulin, J. Favergeon, A. Terlain, M. Tabarant, S. Delpech and G. Picard, *Corrosion Science* **50**, 2008 (2523).

29. G. Müller, G. Schumacher and F. Zimmermann, *Journal of Nuclear Materials* **278**, 2000 (85).
30. P. Hosemann, M. Hawly, D. Koury, J. G. Swadener, J. Welch, A. L. Johnson, G. Mori and N. Li, *Journal of Nuclear Materials* **375**, 2008 (323).
31. E. Yamaki and K. Kikuchi, *Journal of Nuclear Materials* **398**, 2010 (153).
32. K. Kikuchi, A. K. Rivai, S. Saito, A. M. Bolind and A. Kogure, *Journal of Nuclear Materials* **431**, 2012 (120).
33. K. Kikuchi, N. Okada, M. Kato, H. Uchida and S. Saito, *Journal of Nuclear Materials* **450**, 2014 (237).
34. M. Schütze, P. F. Tortorelli and I. G. Wright, *Oxidation of Metals* **73**, 2010 (398).
35. J. Armitt, D. R. Holmes, M. I. Manning, D. B. Meadowcroft, and E. Metcalfe, *The Spalling of Steam Grown Oxide from Superheater and Reheater Tube Steels*, EPRI Report No. FP 686 (1978).
36. P. L. Harrison, *Corrosion Science* **7**, 1967 (789).
37. M. Nagl, W. Evans, D. Hall and S. Saunders, *Journal de Physique IV* **3**, 1993 (933).
38. J. Robertson and M. I. Manning, *Materials Science and Technology* **6**, 1990 (81).
39. X. Zhao, R. M. Langford, J. Tan and P. Xiao, *Scripta Materialia* **59**, 2008 (39).
40. D. E. J. Armstrong, M. E. Rogers and S. G. Roberts, *Scripta Materialia* **61**, 2009 (741).
41. B. L. Boyce, J. R. Michael and P. G. Kotula, *Acta Materialia* **52**, 2004 (1609).
42. Y. Yang, H. H. Ruan, J. Lu, N. Yao, W. L. Shan and W. O. Soboyejo, *Experimental Mechanics* **49**, 2009 (731).
43. D.E.J. Armstrong. PFMC/FEMaS Conference Proceedings (2011).
44. P. Hosemann, J. G. Swadener, J. Welch and N. Li, *Journal of Nuclear Materials* **377**, 2008 (201).
45. Y. Zhao, H. Dai and W. Jin, *Corrosion Science* **65**, 2012 (163).
46. W. C. Oliver and G. M. Pharr, *Journal of Materials Research* **7**, 1992 (1564).
47. K. F. McCarty and D. R. Boehme, *Journal of Solid State Chemistry* **79**, 1989 (19).
48. G. Hilson, K. R. Hallam and P. E. J. Flewitt, *Mat. Sci. Forum* **524–525**, 2006 (957).
49. J. Mougin, N. Rosman, G. Lucazeau and A. Galerie, *Journal of Raman Spectroscopy* **32**, 2001 (739).
50. B.D. Hosterman, Raman spectroscopic study of solid solution spinel oxides, PhD thesis, University of Nevada, Las Vegas, 2011.
51. J. Kim, K. J. Choi, C. B. Bahn and J. H. Kim, *Journal of Nuclear Materials* **449**, 2014 (181).
52. D. Chicot, J. Mendoza, A. Zaoui, G. Louis, V. Lepingle, F. Roudet and J. Lesage, *Materials Chemistry and Physics* **129**, 2011 (862).
53. A. M. Jubb and H. C. Allen, *ACS Applied Materials and Interfaces* **2**, 2010 (2804).
54. O. N. Shebanova and P. Lazor, *Journal of Raman Spectroscopy* **34**, 2003 (845).
55. L. V. Gasparov, D. B. Tanner, D. B. Romero, H. Berger, G. Margaritondo and L. Forro, *Physical Review B* **62**, 2000 (7939).
56. T. Miyazawa, S. Uchida, T. Satoh, Y. Morishima, T. Hirose, Y. Satoh, K. IInuma, Y. Wada, H. Hosokawa and N. Usui, *Journal of Nuclear Science and Technology* **42**, 2005 (233).
57. M. Proy, M. V. Utrilla, E. Otero, B. Bouchaud and F. Pedraza, *Journal of Materials Engineering and Performance* **23**, 2014 (2847).
58. A. Yogi and D. Varshney, *Journal of Advanced Ceramics* **2**, 2013 (360).
59. I. Chamritski and G. Burns, *Journal of Physical Chemistry B* **109**, 2005 (4965).
60. D. Lenaz and V. Lughi, *Physics and Chemistry of Minerals* **40**, 2013 (491).
61. K. R. Elder, K. Thornton and J. J. Hoyt, *Philosophical Magazine* **91**, 2011 (151).
62. D. E. J. Armstrong, A. S. M. A. Haseeb, S. G. Roberts, A. J. Wilkinson and K. Bade, *Thin Solid Films* **520**, 2012 (4369).
63. D. Jauffres, X. Liu and C. L. Martin, *Procedia Engineering* **10**, 2011 (2719).
64. M. G. Mueller, V. Pejchal, G. Žagar, A. Singh and M. Cantoni, *Acta Materialia* **86**, 2015 (385).
65. D. Frazer, M. D. Abad, D. Krumwiede, C. Back, K. Hesham and P. Hosemann, *Composites: Part A* **70**, 2015 (93).